CHALMERS
UNIVERSITY OF TECHNOLOGY

Inner dusty envelope of the AGB stars W Hydrae, SW Virginis, and R Crateris using SPHERE/ZIMPOL

A&A 635, A200 (2020)
https://doi.org/10.1051/0004-6361/201834618

Astronomy & Astrophysics

Inner dusty envelope of the AGB stars W Hydrae, SW Virginis, and R Crateris using SPHERE/ZIMPOL

T. Khouri[1], W. H. T. Vlemmings[1], C. Paladini[2], C. Ginski[3,4], E. Lagadec[5], M. Maercker[1], P. Kervella[6], E. De Beck[1], L. Decin[7], A. de Koter[3,7], and L. B. F. M. Waters[3,8]

[1] Department of Space, Earth and Environment, Chalmers University of Technology, Onsala Space Observatory, 439 92 Onsala, Sweden
e-mail: theo.khouri@chalmers.se
[2] European Southern Observatory, Alonso de Cordova 3107, Vitacura, Santiago, Chile
[3] Astronomical Institute Anton Pannekoek, University of Amsterdam, PO Box 94249, 1090 GE Amsterdam, The Netherlands
[4] Sterrewacht Leiden, PO Box 9513, Niels Bohrweg 2, 2300 RA Leiden, The Netherlands
[5] Laboratoire Lagrange, Université Côte d'Azur, Observatoire de la Côte d'Azur, CNRS, Blvd de l'Observatoire, CS 34229, 06304 Nice cedex 4, France
[6] LESIA, Observatoire de Paris, Université PSL, CNRS, Sorbonne Université, Univ. Paris Diderot, Sorbonne Paris Cité, 5 place Jules Janssen, 92195 Meudon, France
[7] Instituut voor Sterrenkunde, KU Leuven, Celestijnenlaan 200D 2401, 3001 Leuven, Belgium
[8] SRON Netherlands Institute for Space Research, Sorbonnelaan 2, 3584 CA Utrecht, The Netherlands

Received 9 November 2018 / Accepted 25 February 2020

ABSTRACT

Context. The asymptotic giant branch (AGB) marks the final evolutionary stage of stars with initial masses between ~0.8 and 8 $M_{\odot}$. During this phase, stars undergo copious mass loss, which contributes significantly to the enrichment of the interstellar medium. The well-accepted mass-loss mechanism requires radiation pressure acting on dust grains that form in the density-enhanced and extended AGB stellar atmospheres. The details of the mass-loss process are not yet well understood, however. For oxygen-rich AGB stars, which are the focus of this study, the dust grains that drive the wind are expected to scatter visible light very efficiently because their sizes are relative large.

Aims. We study the distribution of dust in the inner wind of oxygen-rich AGB stars to advance our understanding of the wind-driving process.

Methods. We observed light scattered off dust grains that form around three oxygen-rich AGB stars (W Hya, SW Vir, and R Crt) with mass-loss rates between 10^{-7} and 10^{-6} $M_{\odot}$ yr^{-1} using the extreme-adaptive-optics imager and polarimeter SPHERE/ZIMPOL with three filters centred at 0.65, 0.75 and 0.82 μm. We compared the observed morphologies and the spectral dependence of the scattered light between the three sources and determined the radial profile, per image octant, of the dust density distribution around the closest target, W Hya.

Results. We find the distribution of dust to be asymmetric for the three targets. A biconical morphology is seen for R Crt, with a position angle that is very similar to those inferred from interferometric observations of maser emission and of mid-infrared continuum emission. The cause of the biconical outflow cannot be inferred from the ZIMPOL data, but we speculate that it might be the consequence of a circumstellar disc or of the action of strong magnetic fields. The dust grains polarise light more efficiently at 0.65 μm for R Crt and SW Vir and at 0.82 μm for W Hya. This indicates that at the time of the observations, the grains around SW Vir and R Crt had sizes <0.1 μm, while those around W Hya were larger, with sizes $\gtrsim$0.1 μm. The asymmetric distribution of dust around R Crt makes the interpretation more uncertain for this star, however. We find that polarised light is produced already from within the visible photosphere of W Hya, which we reproduce using models with an inner dust shell that is optically thick to scattering. We fit radiative transfer models to the radial profile of the polarised light observed around W Hya and find a steep dust density profile, with steepness varying considerably with direction. We find the wind-acceleration region of W Hya to extend to at least ~7 $R_{\star}$. This is in agreement with theoretical predictions of wind acceleration up to ~12 $R_{\star}$, and highlights that ZIMPOL observations probe the crucial region around AGB stars where dust forms and is accelerated.

Key words. stars: AGB and post-AGB – stars: imaging – stars: mass-loss – circumstellar matter – techniques: polarimetric – techniques: high angular resolution

1. Introduction

At the end of their lives, stars with masses between 0.8 and 8 $M_{\odot}$ present strong mass loss during their evolution on the asymptotic giant branch (AGB). This plays an important role in the enrichment of the interstellar medium (Habing & Olofsson 2003). The mass-loss mechanism is widely accepted to be a two-step process in which stellar pulsations and/or convective motion increase the density scale height of the atmosphere, and radiation pressure acting on newly formed dust grains drives the wind (Höfner & Olofsson 2018). The details of this process are not yet well understood, however, and predicting the mass-loss rate of an AGB star from first principles is not possible at present. For instance, the relative contribution between convection and stellar pulsations in creating the extended AGB atmospheres is not known, and neither is how this balance is affected by stellar properties and

AGB evolutionary phase. Moreover, the dust-formation process is complex, and a detailed modelling of all relevant chemical reactions in the highly dynamical AGB atmospheres is still in its infancy. For oxygen-rich AGB stars (in which the atmospheric carbon-to-oxygen ratio is lower than one), the scenario is particularly complex because opaque dust species that could drive the wind through absorption of photons do not form close enough to the star to trigger the outflow (Woitke 2006). Therefore, the outflows of O-rich AGB stars have been proposed to be driven by radiation pressure caused by scattering of visible and near-infrared light on relatively large ($\gtrsim$0.1 μm) but translucent dust grains (Höfner 2008). High-angular-resolution observations of polarised light toward O-rich AGB stars have revealed that grains with sizes $\gtrsim$0.1 μm indeed exist within a few stellar radii from the central star (Norris et al. 2012; Kervella et al. 2015; Khouri et al. 2016; Ohnaka et al. 2016, 2017).

The nature of the first dust grains to form around O-rich AGB stars is still debated both from an observational (e.g. Zhao-Geisler et al. 2012; Karovicova et al. 2013; Khouri et al. 2015; Kamiński et al. 2016, 2017) and a theoretical perspective (e.g. Gail et al. 2016; Gobrecht et al. 2016; Höfner et al. 2016; Bladh et al. 2017). Nonetheless, observations indicate that aluminium-oxide grains form closer to the star at approximately two stellar radii, while opaque silicates form farther away, at a few times this distance (e.g. Zhao-Geisler et al. 2012; Karovicova et al. 2013). Theoretical models indicate that aluminium oxide might indeed form directly from the gas phase (Gobrecht et al. 2016), but the sizes and the lattice structure of such grains are still a matter of discussion (e.g., Decin et al. 2017). Whether aluminium oxide (Gobrecht et al. 2016), titanium oxide (Plane 2013), or silicates (Gail et al. 2016) are the first species to condense from the gas phase is also still debated. Constraints on the composition of the dust have been actively pursued recently (e.g. Kamiński et al. 2016, 2017; Decin et al. 2017; Khouri et al. 2018), but no conclusion has been reached. Nonetheless, the condensation of some type of silicate grain is deemed necessary for the development of the outflows of O-rich AGB stars because of the relatively low abundance of aluminium (e.g. Bladh & Höfner 2012). A possible scenario is that the first aluminium-oxide grains act as seeds for the subsequent condensation of iron-free silicates (e.g. Kozasa & Sogawa 1997; Höfner et al. 2016), and that iron is incorporated farther out in the outflow (e.g. Bladh et al. 2015). The way in which all these dust properties vary for AGB stars with different characteristics (such as pulsation amplitude and mode, period, and mass-loss rate) is not known either.

In this context, we observed polarised light towards three semi-regular-variable O-rich AGB stars using the Zurich Imaging Polarimeter (ZIMPOL), an extreme adaptive-optics imager and polarimeter of the Spectro-Polarimetric High-contrast Exoplanet Research (SPHERE) on the Very Large Telescope (VLT). In this way, we aim to study the grains expected to drive the outflows using the polarised light they produce through scattering. From these observations, we can study their spatial distribution, and in particular, the radial distance at which they from.

2. Observations

2.1. Description of the observed stars

The three stars we selected are W Hya, SW Vir, and R Crt. These are semi-regular variable O-rich AGB stars that present mass-loss rates ranging from $\sim10^{-7}$ $M_\odot\,\mathrm{yr}^{-1}$ to $\sim10^{-6}$ $M_\odot\,\mathrm{yr}^{-1}$ (see Table 1). We note that ZIMPOL observations of AGB stars indicate strong variability on timescales of one month (Khouri et al. 2016; Ohnaka et al. 2017), and the observed differences between sources based on single-epoch observations should therefore be interpreted with care and need to be followed up.

Table 1. Observed sources.

Source	d [pc]	$\theta_\star$ [mas]	P [days]	$V_{\max}$ [mag]	ΔV [mag]	$\dot{M}$ [$M_\odot\,\mathrm{yr}^{-1}$]
W Hya	98 [(a),(b)]	50 [(c)] / 41 [(d)] / 80 [(e)]	388 [(e)]	6.0	4.0	1×10^{-7} [(f)]
SW Vir	143 [(b)]	/ 16.8 [(g)] /	150 [(h)]	6.2	1.8	4×10^{-7} [(h)]
R Crt	260 [(b)]	/ 18 / 38 [(i)]	160 [(h)]	9.8	1.4	8×10^{-7} [(h)]

Notes. Stellar diameters $\theta_\star$ given at visible, near-infrared, and 8.0 μm, when available.
References. (a) Vlemmings et al. (2003), (b) van Leeuwen (2007), (c) Ireland et al. (2004), (d) Woodruff et al. (2009), (e) Zhao-Geisler et al. (2011), (f) Khouri et al. (2014a), (g) White & Feierman (1987), (h) Olofsson et al. (2002), and (i) Paladini et al. (2017).

2.1.1. W Hya

At a distance of ≈100 pc (Vlemmings et al. 2003; van Leeuwen 2007), W Hya is the second brightest star in the K band and one of the brightest infrared sources in the sky (Wing 1971). Its visual magnitude varies between ∼6 mag and 9 mag in about 388 days (Zhao-Geisler et al. 2011). A mass-loss rate between 10^{-7} and 1.5×10^{-7} $M_\odot$ yr^{-1} is found based on models for CO emission lines (e.g. Maercker et al. 2008; Khouri et al. 2014a), while a main-sequence mass between 1.0 and 1.5 $M_\odot$ has been derived from studies of oxygen isotopic ratios (Khouri et al. 2014b; Danilovich et al. 2017). The stellar radius varies in time and strongly with wavelength (Zhao-Geisler et al. 2011). To our knowledge, the smallest radius of ∼15 mas was reported by Woodruff et al. (2009) based on observations in the near-infrared at pulsation phase 0.8. Throughout the paper, we consider a reference stellar radius ($R_\star$) of 18 mas as measured by Woodruff et al. at pulsation phase 0.54, which is similar to when the observations presented by us were acquired (0.5).

Observations of scattered light using the Nasmyth Adaptive Optics System Near-Infrared Imager and Spectrograph (NaCo) on the VLT in March 2009 and June 2010 (Norris et al. 2012) and using ZIMPOL in July 2015 (Ohnaka et al. 2016) and March 2016 (Ohnaka et al. 2017) show a dust envelope containing large dust grains (with radii $\gtrsim$0.1 μm) with an inner radius of 25 mas (Ohnaka et al. 2016), 34 mas (Ohnaka et al. 2017) and 37 mas (Norris et al. 2012) at phases 0.92, 0.54, and 0.2, respectively. Whether the grains observed through scattered light are aluminium oxide or silicates is still unclear (e.g. Ohnaka et al. 2017). Interferometric infrared observations reveal that amorphous aluminium oxide emission is produced close to the star, within ∼50 mas (5 au) in radius, while silicate emission arises much farther out, at $r\gtrsim400$ mas (40 au, Zhao-Geisler et al. 2011). By studying the infrared spectrum of W Hya, Khouri et al. (2015) found that emission from amorphous aluminium oxide must originate almost exclusively by material that is gravitationally bound to the star.

Recent images of the sub-millimeter continuum emission of W Hya acquired using the Atacama Large Millimeter/submillimeter Array (ALMA) at pulsation phase 0.3 (March 2015) revealed an asymmetric source with size 50.9×56.5 mas and an unresolved hotspot on the surface. The same data show that the extended atmosphere of W Hya, traced by the $v=1, J=3-2$ CO line, extends out to ≈48 mas (4.8 au) in radius (Vlemmings et al. 2017), tracing the extended atmosphere. The

grains that produce the scattered light might therefore also be present in the high-gas-density environment of the extended atmosphere that is gravitationally bound to the star. An independent analysis of these ALMA observations suggests aluminium to be highly depleted into dust in the inner regions and silicon not to be significantly depleted (Takigawa et al. 2017). We note that the simplified model employed by Takigawa et al. is most likely not applicable to the innermost regions of the circumstellar envelope probed by the ALMA observations, and their results must be confirmed by more detailed calculations.

2.1.2. R Crt

R Crt is a semi-regular variable (type SRb) with a pulsation period of 160 days and a visual magnitude amplitude of 1.4 mag (Jura & Kleinmann 1992). Its reported distance varies from ~170 pc (Bowers & Johnston 1994) to 261^{+86}_{-42} pc (van Leeuwen 2007). Based on observations of low-excitation CO lines, Olofsson et al. (2002) found R Crt to have the highest mass-loss rate ($\sim 8 \times 10^{-7}$ $M_\odot\,\mathrm{yr}^{-1}$) of the 43 nearby semi-regular variables in their sample, with an expansion outflow velocity of 10.6 $\mathrm{km\,s}^{-1}$. A diameter – V–K relation (van Belle et al. 1999) predicts a K-band diameter of 19 mas. However, a fit to archive VINCI (on the VLT interferometer) data using a uniform disc source model provides a slightly smaller solution, with a K-band diameter of about 14.8 ± 0.2 mas. Observations of R Crt using MIDI on the VLTI in the mid-infrared and at short baselines (with a resolution of ~68 mas) are best fit using an elliptical Gaussian model with an axis ratio of 0.7 and a position angle of 157° (Paladini et al. 2017). At the wavelengths of the MIDI observations, circumstellar dust becomes a significant source of opacity. This means that the dust distribution might affect the measurement, but the extent to which this occurs is not yet clear. In the far-infrared and on a larger scale, a dust shell with radius of a few arcminutes is seen both in IRAS (Young et al. 1993) and *Herschel*/PACS (Cox et al. 2012) images. This shell is probably created by the interaction between the stellar outflow and the interstellar medium (ISM).

R Crt presents SiO, H_2O, and OH maser emission. VLBI maps of the 22 GHz water maser (Ishitsuka et al. 2001) reveal a biconical outflow at a position angle of 136° (measured from north to east) at $r \lesssim 100$ mas (~5 $R_\star$) from the star. More recent simultaneous observations of SiO and H_2O masers show that the SiO maser spots form a ring, which is typical for AGB stars, with a radius of ~13 mas. The H_2O maser is produced almost exclusively in the south-east with respect to the star, with no emission in the north and north-west regions (Kim et al. 2018). The OH masers were mapped by Szymczak et al. (1999), revealing a displacement between the red- and blue-shifted masers in the same direction as the possible biconical H_2O outflow. Additionally, the size of the OH shell inferred from these observations implies a mass-loss rate one order of magnitude lower than that obtained from CO observations. The magnetic field direction derived from the OH masers is in the same direction (with position angle ~140°). Finally, Herpin et al. (2006) observed the polarisation of the SiO masers and found that the magnetic field (of up to ~3.7 G) is aligned in the same position angle as the OH masers. This suggests that the magnetic field might be related to the asymmetries seen in the star and in the dust and maser distributions.

2.1.3. SW Vir

At a distance of 143^{+20}_{-15} pc (van Leeuwen 2007), SW Vir presents a period of ≈154 days, possibly additional periods of 164 and 1700 days (Percy et al. 2001; Kiss et al. 1999), and a visual magnitude amplitude of ~1.5 mag (Jura & Kleinmann 1992). The detection of Tc in the atmosphere shows that SW Vir is in the thermally pulsating AGB phase (Lebzelter & Hron 2003). Models fitting observations of low-excitation CO lines indicate a mass-loss rate of 4×10^{-7} $M_\odot$ yr^{-1} and an expansion velocity of the outflow of 7.5 $\mathrm{km\,s}^{-1}$ (Olofsson et al. 2002). The uniform disc diameter of SW Vir has been measured in the H (Ridgway et al. 1982) and K (Schmidtke et al. 1986) bands to be 16.8 mas and 16.7 mas, respectively.

2.2. Data acquisition and data reduction

W Hya, SW Vir, and R Crt were observed using ZIMPOL in three filters: *NR* ($\lambda_c = 0.65$ μm), *cnt748* ($\lambda_c = 0.75$ μm), and *cnt820* ($\lambda_c = 0.82$ μm), with λ_c the central wavelength of the filter. The filters *NR*, *cnt748*, and *cnt820* have spectral widths of 56.7, 20.6, and 19.8 nm, respectively. The ESO ID for the observation programme is 096.D-0930. R Crt was observed in December 2015 and January 2016, while W Hya and SW Vir were observed in March 2016. The exposure time per source per filter varied between 15 min and roughly one hour. SW Vir saturated the detector in the observations using filters *cnt748* and *cnt820*. We therefore also acquired images with the use of a neutral density filter that blocks ~92% of the stellar light (ND1). Each observing cycle consists of four loops to obtain the images Q_+, Q_-, U_+, and U_-, with the half-wave plate oriented at 0°, 22.5°, 45°, and 67.5° with respect to the north direction, respectively. In each loop, a number of images, NDIT, was acquired with a given detector integration time, DIT. The whole cycle was repeated several times for each filter until the total exposure time was reached. Observations of a reference star to obtain the point spread function (PSF) were carried out following the observations of the science target for each filter. In Table 2 we give the exposure and detector integration times for each filter, as well as the airmass and visible seeing at the time of each observation and the H-band Strehl ratio in the obtained images. The details of the observations of the PSF-reference sources are also given. The Strehl ratio at the wavelengths of a given ZIMPOL image (S_λ) was calculated from the H-band Strehl ratio using the Maréchal approximation, as done by Adam & Ohnaka (2019) for ZIMPOL observations of IK Tau following Lawson (2000). In this way, S_λ is given by

$$S_\lambda = \exp\left[\left(\frac{\lambda_\mathrm{H}}{\lambda}\right)^2 \times \ln(S_\mathrm{H})\right],$$

where $\lambda_\mathrm{H} = 1.65$ μm. The values obtained are given in Table 2 for each observation.

The data were reduced using the (SPHERE/ZIMPOL) SZ-software package developed at the Eidgenössische Technische Hochschule, Zurich. The basic procedures are standard for astronomical imaging (bias frame subtraction, cosmic ray removal, and flat fielding; see e.g. Schmid et al. 2017) and equivalent to those carried out using the SPHERE DRH-software provided by ESO. The images of the Stokes parameters Q, U, and I were created using

$$Q = \frac{Q_+ - Q_-}{2},\ U = \frac{U_+ - U_-}{2} \text{ and } I = \frac{Q_+ + Q_- + U_+ + U_-}{4}.$$

The polarisation observations also require a calibration of the polarimetric modulation-demodulation efficiency of ZIMPOL. This was done by dividing the observed Q and U images by

Table 2. Observation log containing the filter, dates, and exposure times of observations together with other details regarding the observations and derived values.

Source	Filter	Obs. date	Exp time [min]	DIT[s] × NDIT	AM	θ ["]	S_H	S_λ	$FWHM_\star$ [mas] [deg]	$FWHM_\star^{Mod}$ [mas] [deg]	Peak PD [%]
W Hya	*NR*	01-Mar.-16	32.0	1.2 × 20	1.09	0.88–1.12	0.81	0.25	69.1 × 71.8 (165)	63.6 × 66.6 (146) (†)	16.6
	cnt748	08-Mar.-16	24.0	1.2 × 20	1.03	0.74–1.16	0.92	0.67	63.7 × 69.0 (160)	58.9 × 64.4 (159) (†)	18.5
	cnt820	08-Mar.-16	24.0	1.2 × 20	1.03	0.74–1.16	0.92	0.71	56.4 × 62.2 (150)	50.2 × 56.3 (148) (†)	20.2
HD 123906	*NR*	01-Mar.-16	8.6	1.2 × 18	1.1	0.98–1.12	0.68	0.08	36.7 × 40.1 (9)		
HD 118877	*cnt748*	08-Mar.-16	5.8	1.2 × 12	1.1	0.9–1.15	0.72	0.20	27.3 × 30.8 (173)		
	cnt820	08-Mar.-16	5.8	1.2 × 12	1.1	0.9–1.15	0.72	0.26	28.0 × 31.8 (173)		
SW Vir	*NR*	09-Mar.-16	34.6	1.2 × 18	1.1	0.76–0.88	0.90	0.50	29.1 × 31.3 (10)	12.1 × 16.3 (117)	9.5
	cnt748	10-Mar.-16	15.4	1.2 × 16	1.12	0.77–0.91	0.90	0.60	–	–	8.5
	cnt820	10-Mar.-16	15.4	1.2 × 16	1.12	0.77–0.91	0.90	0.65	–	–	7.0
	cnt748	10-Mar.-16	17.9	2.8 × 16	1.17	1.15–1.93	0.89	0.57	28.2 × 29.7 (175)	14.8 × 16.1 (174)	8.1
	cnt820	10-Mar.-16	17.9	2.8 × 16	1.17	1.15–1.93	0.89	0.62	28.2 × 29.8 (173)	12.2 × 13.5 (173)	6.4
p Vir	*NR*	09-Mar.-16	9.6	4.0 × 6	1.1	1.03–1.18	0.82	0.27	24.2 × 28.8 (18)		
	cnt748	10-Mar.-16	6.0	5.0 × 6	1.1	1.02–1.18	0.86	0.48	24.1 × 24.9 (177)		
	cnt820	10-Mar.-16	6.0	5.0 × 6	1.1	1.02–1.18	0.86	0.54	25.4 × 26.6 (172)		
R Crt	*NR*	19-Dec.-15	64.0	5.0 × 16	1.2	0.73–0.97	0.83	0.30	35.5 × 38.1 (9)	21.4 × 23.9 (4)	8.5
	cnt748	08-Jan.-16	24.0	1.2 × 20	1.3	0.88–1.18	0.71	0.19	37.3 × 42.4 (147)	24 × 31 (142)	6.0
	cnt820	08-Jan.-16	24.0	1.2 × 20	1.3	0.88–1.18	0.71	0.25	35.2 × 40.2 (153)	20.1 × 26.5 (145)	4.0
HD 96364	*NR*	19-Dec.-15	7.7	1.2 × 16	1.2	0.68–0.89	0.81	0.25	28.3 × 29.8 (17)		
	cnt748	08-Jan.-16	5.6	2.0 × 14	1.2	0.86–0.95	0.72	0.20	28.1 × 29.5 (167)		
	cnt820	08-Jan.-16	5.6	2.0 × 14	1.2	0.86–0.95	0.72	0.26	28.5 × 30.5 (174)		

Notes. The observations of SW Vir for which a neutral density filter (*ND1*) was used are marked using italic font for the filter name. DIT is the exposure time of the individual frames, and NDIT is the number of frames per exposure. Each cycle (DIT × NDIT) was repeated four times to obtain $+Q$, $-Q$, $+U$, and $-U$ frames, and the whole cycle was repeated several times for each filter and epoch until the total exposure time was reached. AM and θ are the airmass and the visible seeing at the time of the observations, and S_H and S_λ are the Strehl ratios observed at the H-band and this ratio calculated at the observed wavelength (see Sect. 2.2), respectively. $\lambda_\circ$ and $\Delta\lambda$ are the central wavelength and the FWHM of the filters used. $FWHM_\star$ and $FWHM_{PSF}$ are the FWHM obtained by fitting a 2D Gaussian to the observed images of the science targets and the PSF references, while $FWHM_\star^{Mod}$ is the FWHM of the model Gaussian star that best fits the observations. The position angle of the Gaussian ellipse is given in parentheses after the minor and major values of the FWHM. Peak PD is the observed peak value of the polarisation degree. (†) - For W Hya, we used the observations of p Vir as the PSF reference for the fitting procedure (see text).

the polarisation efficiency (typically ~80% for fast polarimetry observations; SPHERE manual version 101). We performed this correction using the images for the polarisation efficiency calibration provided in the ESO archive and calculating a mean value of the polarisation efficiency over the image. This was done to minimise noise introduced by image division. The polarisation intensity, I_p, polarisation degree, p, and direction of the polarisation vectors with respect to the north direction, θ, were calculated using

$$I_p = \sqrt{Q^2 + U^2},\ p = \frac{I_p}{I} \text{ and } \theta = \frac{\arctan(U/Q)}{2}.$$

At the time of the observations, the atmospheric wind speeds at the VLT site were always $\gtrsim$6 m s^{-1}. This guarantees that the low-wind effect, which can significantly degrade the obtained PSF, does not affect the observations we present (see Schmid et al. 2018).

The pulsation phase of W Hya was 0.5 (minimum light) when the ZIMPOL observations we report were taken. The low-amplitude and irregular light curves of SW Vir and R Crt make it difficult to define their pulsation phases at the time of the ZIMPOL observations.

3. Observational results

3.1. Total intensity images

The SPHERE/ZIMPOL images resolve the stellar discs of the nearest AGB stars at the ~25–30 mas scale. In the observations that we report, W Hya is clearly resolved, R Crt is marginally resolved, and SW Vir is not resolved. We determined full width at half maximum (FWHM) stellar sizes by fitting Gaussian stellar models to the total intensity images of the three stars using the respective PSF reference images. This was done by approximating the reference PSF by a 2D Gaussian and using the `imfit` routine in the Common Astronomy Software Applications (CASA, McMullin et al. 2007) package. Our results are listed in Table 2. All the images presented in the paper are the direct result of the reduction process, and no additional deconvolution procedure was applied to the data.

3.1.1. W Hya

The total intensity (Stokes I) images reveal an asymmetric source with significant structure, with an emission peak in a bean-shaped region in the north-west (see Fig. 1). The morphology of W Hya is very similar in filters *NR* and *cnt748*, even though the

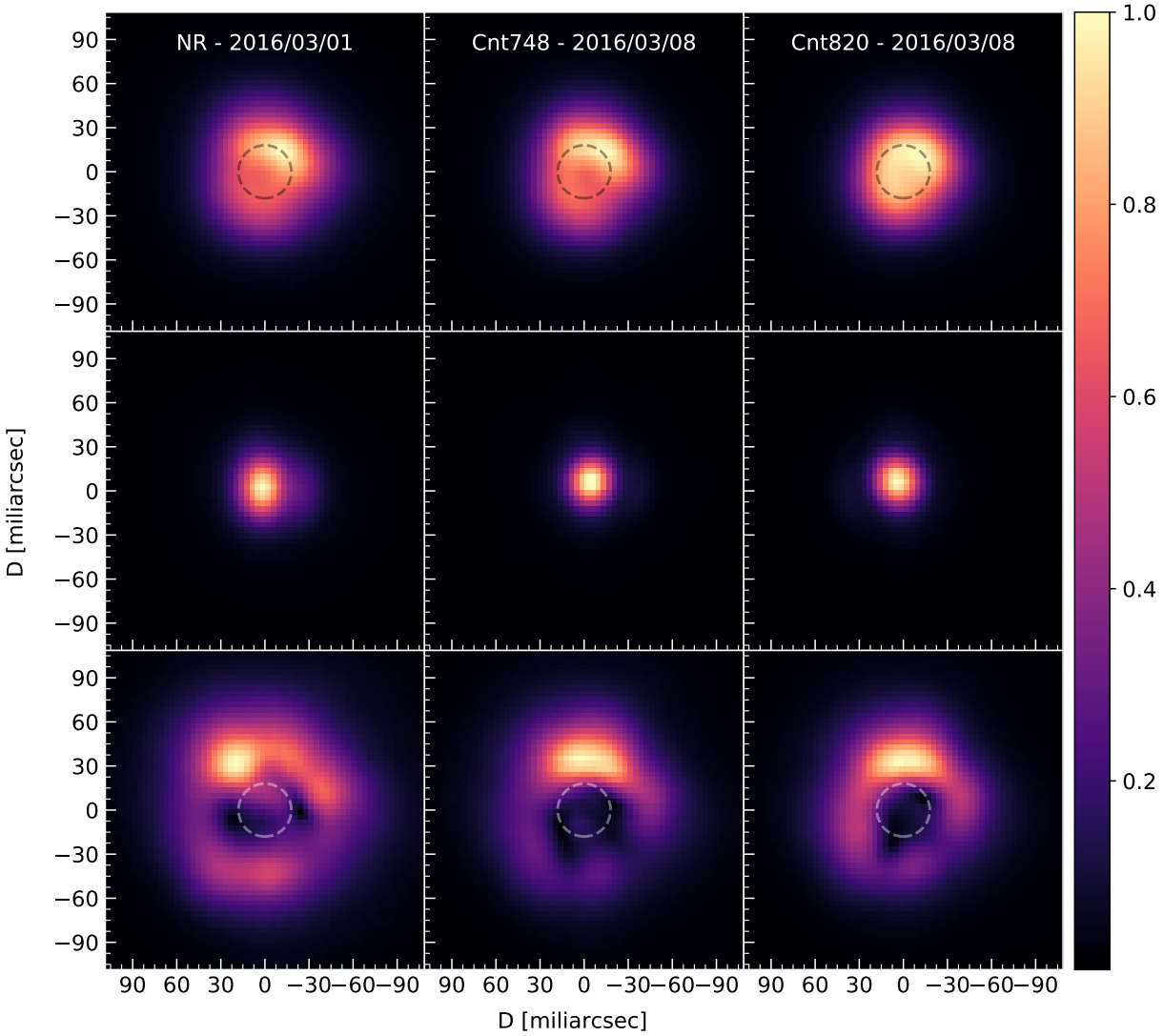

Fig. 1. ZIMPOL observations of W Hya in filters *NR*, *cnt748*, and *cnt820*. *Top panels*: total intensity of W Hya normalised to the peak total intensity value in the image. *Middle panels*: images of the PSF-reference star HD 123906 normalised to the peak polarised intensity. *Bottom panels*: images of the polarised intensity of W Hya normalised to the peak polarised intensity value in the image. The dashed circles indicate the radius of 18 mas measured by Woodruff et al. (2009) in the near-infrared.

images in these filters were obtained one week apart. The asymmetry is less prominent, but still obvious, in the image in filter *cnt820*. Ohnaka et al. (2017) found very similar morphologies of W Hya based on independent ZIMPOL observations taken about two to three weeks later than those reported here.

The PSF reference for the observations in *NR* is broader than those in *cnt748* and *cnt820*, probably because of the different conditions when these observations were carried out. Moreover, a significantly lower Strehl ratio is retrieved from the images of the PSF-references stars of W Hya than from those of W Hya itself. This suggests that the adaptive-optics system did not perform the same for the observations of the science target and the reference stars in this case. Although the observations of p Vir were acquired on different days, they show Strehl ratios much more similar to those of W Hya. The more comparable Strehl ratios between the images of W Hya and p Vir make p Vir a better suited PSF reference. This is also confirmed by our more detailed analysis of W Hya presented in Sect. 4.2.1. We therefore used the observations of p Vir as reference for the PSF in the analysis of W Hya throughout the paper. For reference, we infer the FWHM stellar size of W Hya to be between 5 and 10% smaller when considering the PSF-reference stars observed close in time to W Hya than when considering p Vir.

Based on the FWHM stellar sizes obtained using CASA, we find that the FWHM size of the stellar disc decreases from roughly 65 mas in filter *NR* to roughly 53 mas in filter *cnt820*. This difference is expected to reflect the lower molecular opacity in the wavelength range of filter *cnt820*. From our model calculations presented in Sect. 4.2.1, we derive a uniform stellar disc with a diameter of ~69 mas by fitting the total intensity images at 0.82 μm. Although this value differs significantly from the FWHM derived for a Gaussian stellar disc, this is expected because these two quantities are not directly comparable because the assumed stellar disc models are different.

Vlemmings et al. (2017) derived the uniform stellar disc size of W Hya to be 50.9×56.5 mas in the sub-millimeter at pulsation phase 0.3. Therefore W Hya appears larger at visible wavelengths (>69 mas) than at 338 GHz even when the difference in pulsation phase is considered. Ireland et al. (2004) measured the size of the stellar disc of W Hya to be between 0.68 and 0.93 μm at phase 0.44. The authors reported FWHM sizes of 60 mas at 0.68 μm, 52 mas at 0.75 μm, and

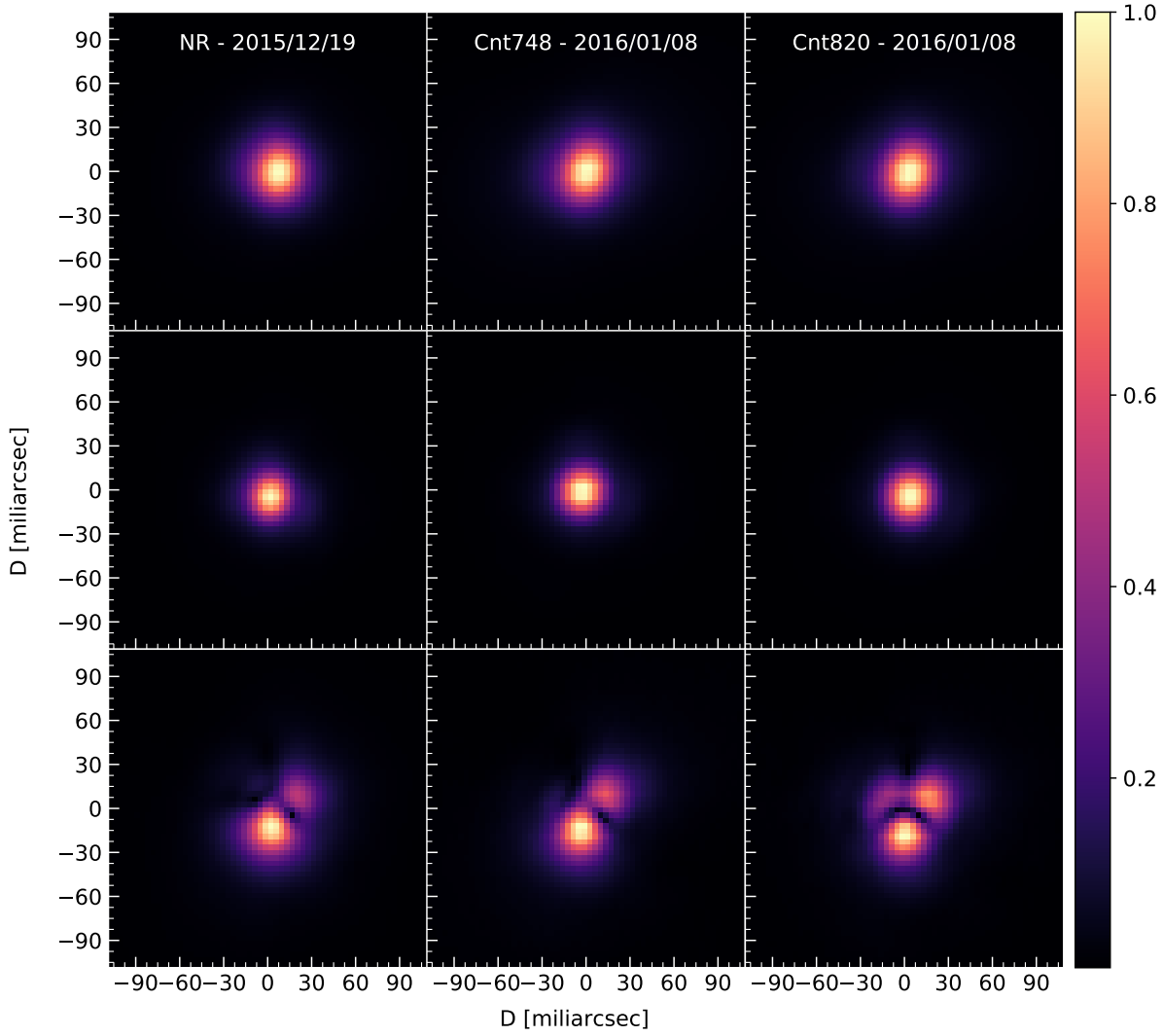

Fig. 2. ZIMPOL observations of R Crt in filters *NR*, *cnt748*, and *cnt820*. *Top panels*: total intensity observed towards R Crt normalised to the peak intensity. *Middle panels*: images of the PSF-reference star HD 96364 normalised to the peak intensity. *Bottom panels*: polarised intensity observed towards R Crt normalised to the peak polarised intensity. The dark stripes seen in the centre appear in the regions where the total intensity peaks and do not correspond to physical features.

42 mas at 0.82 μm, using Gaussian stellar discs. The FWHMs at 0.75 μm and 0.82 μm are significantly smaller than what we find. The filter *NR* covers the spectral region between 0.617 and 0.674 μm and therefore does not overlap with the region observed by Ireland et al. (2004). The observations presented by Ireland et al. (2004) and by us where acquired at similar pulsation phases, but the size of W Hya at a given pulsation phase seems to vary significantly between pulsation cycles. We note again that the Gaussian source model used by Ireland et al. (2004) and us oversimplifies the source morphology, especially for well-resolved observations as those we present.

3.1.2. R Crt

The source size is comparable to the resolution of the ZIMPOL images and is therefore marginally spatially resolved. The Gaussian stellar disc obtained from the fitting procedure reveals an elliptical morphology of R Crt in the total intensity images in filters *cnt748* and *cnt820* with a ratio between the short and long axis ~0.76 and a position angle of 145° ± 8°. These values are consistent with those obtained based on mid-infrared observations using MIDI of 0.7 at a position angle of 157° (Paladini et al. 2017). The elongation of the stellar disc we report is already evident in the total intensity images presented in Fig. 2. The direction of the elongation is also consistent with that measured by Ishitsuka et al. (2001) for a position angle of 136° of the biconical outflow traced by H_2O masers. Interestingly, the total intensity image in filter *NR* does not show an elongated source. The observations in filter *NR* were acquired 20 days before those in the other two filters. It is not clear from the data at hand whether this difference is caused by variability of the source, wavelength dependence of the morphology, or instrumental effects when some of the observations were acquired.

3.1.3. SW Vir

The fitting procedure indicates that the stellar disc of SW Vir is unresolved in the obtained images and its FWHM is roughly between 12 and 16 mas. This is similar to the stellar size measured in the near-infrared (Ridgway et al. 1982; Schmidtke et al. 1986; Mondal & Chandrasekhar 2005) and differs from what we find for W Hya and R Crt, which appear significantly larger in

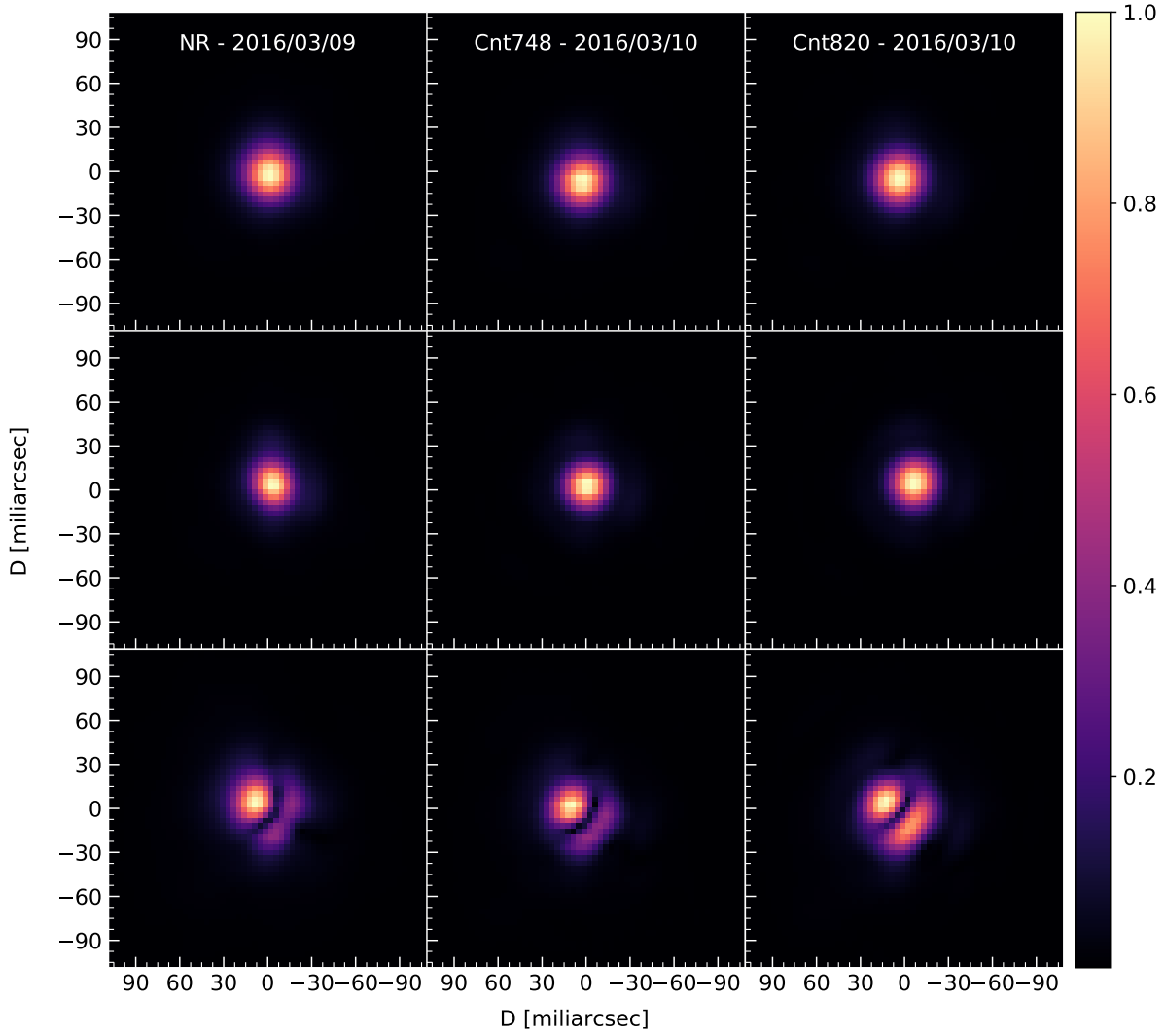

Fig. 3. ZIMPOL observations of SW Vir in filters *NR*, *cnt748*, and *cnt820*. *Top panels*: total intensity observed towards SW Vir normalised to the peak intensity image. *Middle panels*: images of the PSF-reference star p Vir normalised to the peak intensity in the image. *Bottom panels*: polarised intensity observed towards SW Vir normalised to the peak polarised intensity in the image.

the visible than in the near-infrared. The total intensity images of SW Vir show strong PSF diffraction rings. This is not apparent in the total intensity images shown in Fig. 3, but can be clearly seen in the images of the polarisation degree. These diffraction rings are very prominent because SW Vir is very bright, spatially unresolved in the observations, and was observed in relatively narrow-band filters. This produces a strong diffraction pattern that remains prominent because of the small wavelength range probed. As expected, the effect is stronger the narrower the filter used in the observation. Hence, it is stronger in filters *cnt748* and *cnt820* than in filter *NR*.

3.2. Polarised light

The ZIMPOL observations show large amounts of polarised light, $I_{\rm p}$, towards the three sources. For all stars, the scattered light observations show that dust grains form already at $r \lesssim 2\,R_\star$. The polarisation vectors mostly have tangential directions, as expected for an optically thin envelope irradiated by a central source (see Figs. 4, 5, and 6). In the case of SW Vir, this pattern is disrupted by strong PSF rings (see Sect. 3.1.3). The polarised light arises from a region consistent with condensation of either aluminium oxide or Fe-free silicate dust (Höfner et al. 2016). Models for dust formation and growth predict aluminium oxide grains to reach sizes $\gtrsim$0.1 μm, comparable to those of silicates. Aluminium oxide grains might therefore also be expected to produce polarised visible light. However, recent results based on observations of gas and dust suggest that aluminium oxide grains might be smaller than predicted by wind-driving models (Decin et al. 2017; Khouri et al. 2018). Because the scattering properties of the relevant dust species are only weakly dependent on grain composition, constraining the composition of grains seen through scattered light is not possible from the polarised-light images. Combining observations using ZIMPOL with high-angular-resolution observations of the gas (e.g. using ALMA) or dust thermal emission (e.g. using the VLTI) is probably the best way to constrain the composition of these grains (such as the analysis of Mira based on ALMA and ZIMPOL observations by Khouri et al. 2018).

A comparison between the images of the polarisation degree, p, for the three sources (see Figs. 4, 5, and 6) reveals that as the wavelength of observation increases, the polarisation degree also increases for W Hya, while it decreases for R Crt and SW Vir. These different trends are also clear when we consider only

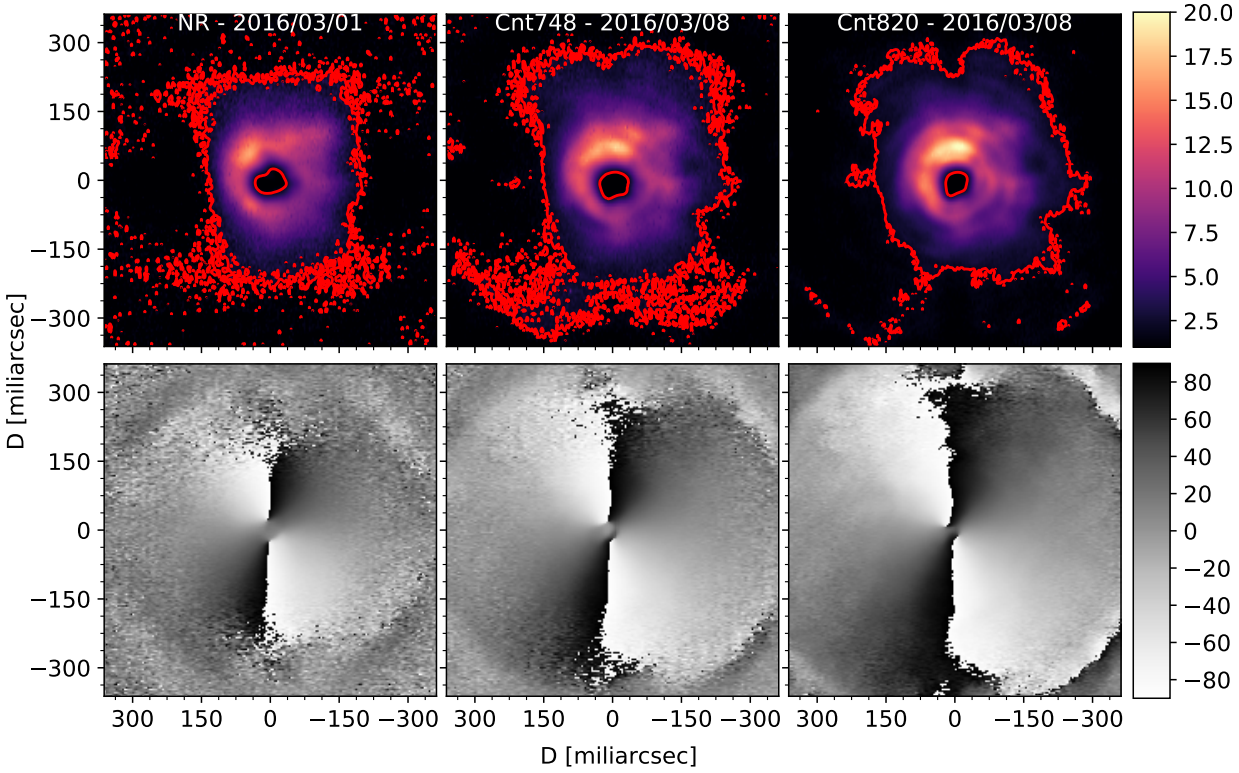

Fig. 4. Polarised light in the close environment of W Hya in filters *NR*, *cnt748*, and *cnt820*. *Upper panels*: colour maps showing the percentage polarisation degree observed toward W Hya in filters *NR*, *cnt748*, and *cnt820* (*from left to right*). The red contours show the 2% level of the polarisation degree below which instrumental polarisation can dominate. *Bottom panels*: grey-scale maps showing the polarisation angle in degrees with respect to the north direction measured in filters *NR*, *cnt748*, and *cnt820* (*from left to right*).

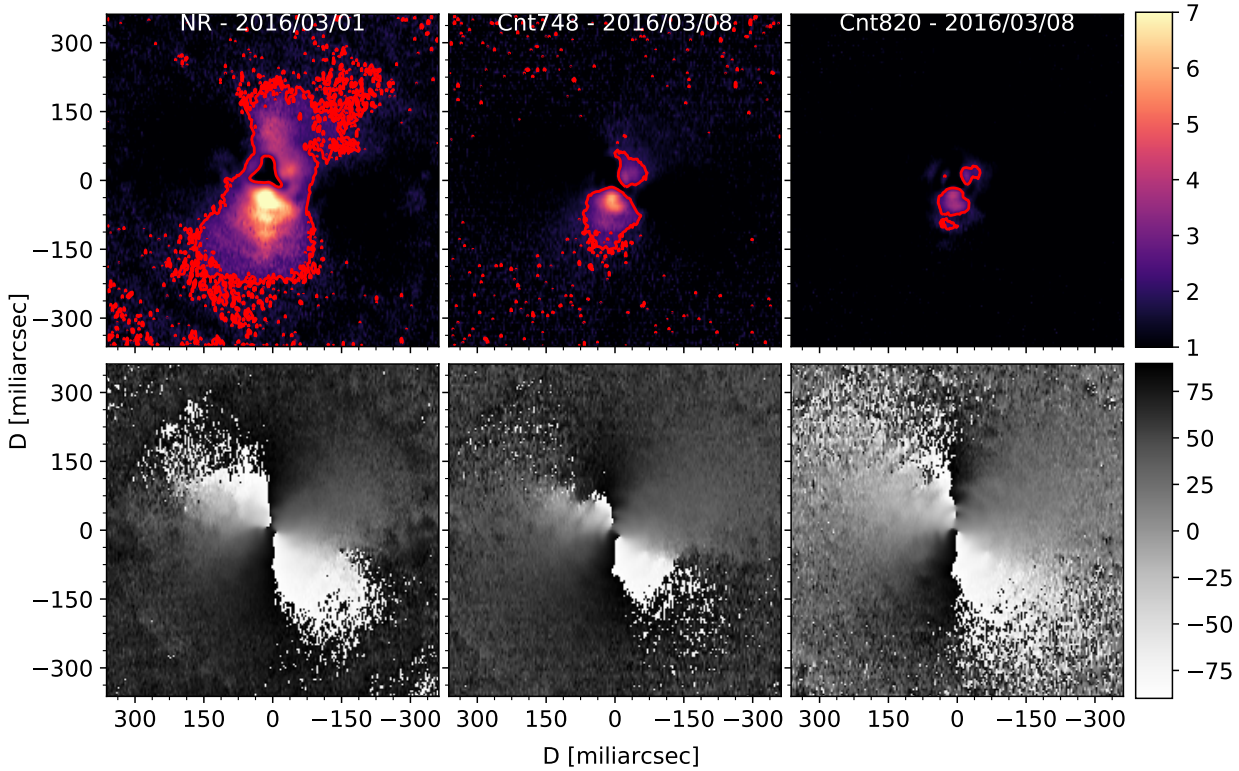

Fig. 5. Polarised light in the close environment of R Crt in filters *NR*, *cnt748*, and *cnt820*. *Upper panels*: colour maps showing the percentage polarisation degree observed towards R Crt in filters *NR*, *cnt748*, and *cnt820* (*from left to right*). The red contours show the 2% level of the polarisation degree below which instrumental polarisation can dominate. *Bottom panels*: grey-scale maps showing the polarisation angle in degrees with respect to the north direction measured in filters *NR*, *cnt748*, and *cnt820* (*from left to right*).

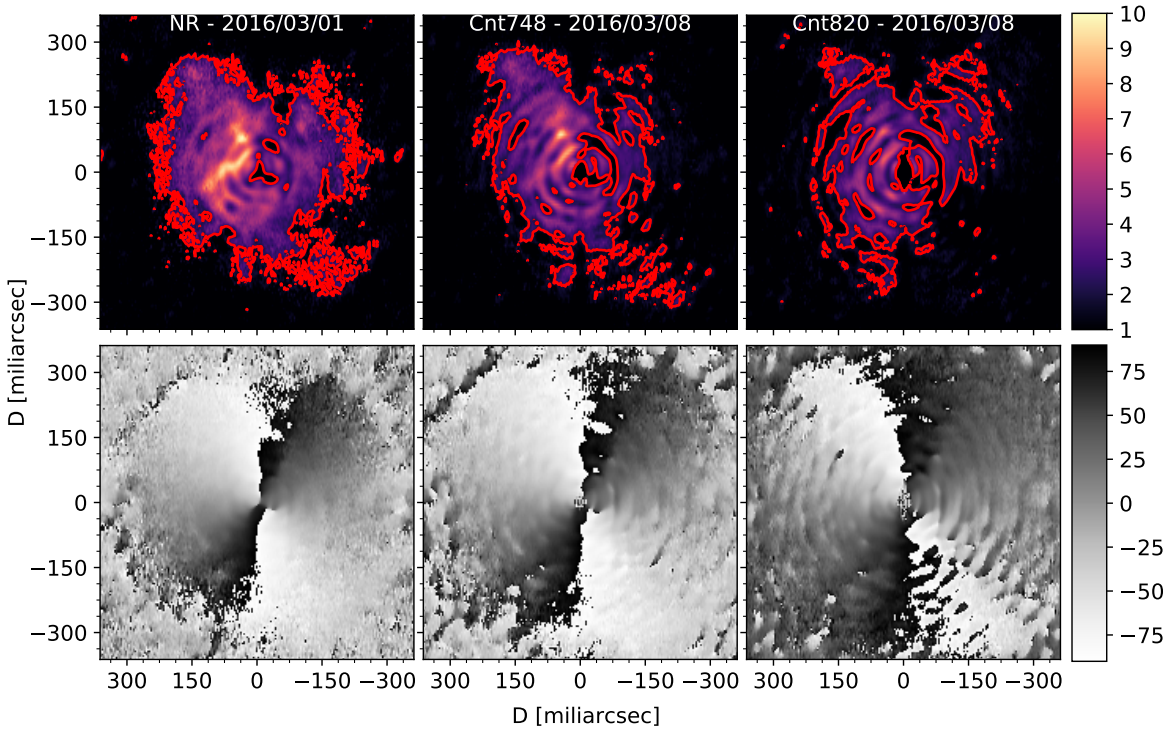

Fig. 6. Polarised light in the close environment of SW Vir in filters *NR*, *cnt748*, and *cnt820*. *Upper panels*: colour maps showing the percentage polarisation degree observed towards SW Vir in filters *NR*, *cnt748*, and *cnt820* (*from left to right*). The red contours show the 2% level of the polarisation degree below which instrumental polarisation can dominate. *Bottom panels*: grey-scale maps showing the polarisation angle in degrees with respect to the north direction measured in filters *NR*, *cnt748*, and *cnt820* (*from left to right*).

the images obtained using filters *cnt748* and *cnt820* that were acquired simultaneously for each source. This means that different sky conditions at the times of observations cannot be invoked to explain the observed difference. Moreover, the resolution of the images is similar in all filters (but lower in filter *NR* for our observations) and cannot be invoked either to explain the decrease in polarisation degree. Therefore we conclude that the different wavelength dependence reflects intrinsic differences between the three sources at the time of the observations. We note that the observed maxima polarisation degrees differ between the three filters at most by ∼20, ∼35, and ∼110% towards W Hya, SW Vir, and R Crt, respectively.

In this type of observations, the performance of the adaptive-optics system is very important in determining how much polarised light is recovered. The polarised intensity decreases for deteriorating resolution because opposite polarisation vectors cancel out within a given resolution element. As an example, we convolved images of model envelopes obtained using the radiative transfer code `MCMax` (see Sect. 4.2, Min et al. 2009) with the PSF-references observed for R Crt, SW Vir, and W Hya in filter *NR* and find that the integrated polarised fluxes measured after convolution decrease to 50, 44, and 33%, respectively, with respect to the original value of a model with one-pixel (3.6×3.6 mas^2) resolution. As mentioned above, the sky conditions became worse between the observations of W Hya and those of the PSF-reference sources. Therefore, the amount of polarised intensity lost is probably smaller in the observations of W Hya than the original PSF-reference stars. Nonetheless, this illustrates how the resolution element of the observations (with respect to the size of the emission region) affect the amount of polarised light retrieved, and the difficulty in directly comparing observations of different sources directly from observed values.

3.2.1. W Hya

The surface brightness distribution of polarised light measured towards W Hya is not symmetric. Moreover, while the images in filters *cnt748* and *cnt820* obtained simultaneously are fairly similar, the image in filter *NR* obtained one week earlier is somewhat different from those by showing, for instance, peak emission at a difference location. In the image in filter *NR*, the polarised intensity peaks in the north-east region, and in those in the *cnt748* and *cnt820* filters, it has a broader peak in the north region (see Fig. 4). Observations by Ohnaka et al. (2017) using ZIMPOL do not show similar differences in morphology. These data were acquired about two to three weeks later than those we report. This suggests that the difference we find in the brightness distribution of the polarised intensity between filter *NR* and filters *cnt748* and *cnt820* is either a consequence of time variability, or, more likely, caused by the poorer resolution in the NR image (see Table 2).

We find that the polarised intensity peaks at smaller radii in the image in filter *cnt820* than it does in the images in filters *cnt748* and *NR*. This comparison is not straightforward, however, because defining the central pixel in the three images is not obvious, and for a given direction, the difference is only about one pixel. These two factors make it difficult to make a comparison as a function of azimuthal angle. Nonetheless, we are able to conclude that the polarised intensity peaks on average about one pixel (3.6 mas, or 0.35 au for at distance of 98 pc) farther away from the central star on average in the images in filters *NR* and *cnt748* than it does in the images in filter *cnt820*. This can be seen from the radial plots in Fig. 7. As discussed by Khouri et al. (2016), this might be caused by increasing scattering optical depths from *cnt820* to *cnt748* to *NR* or by the stronger molecular

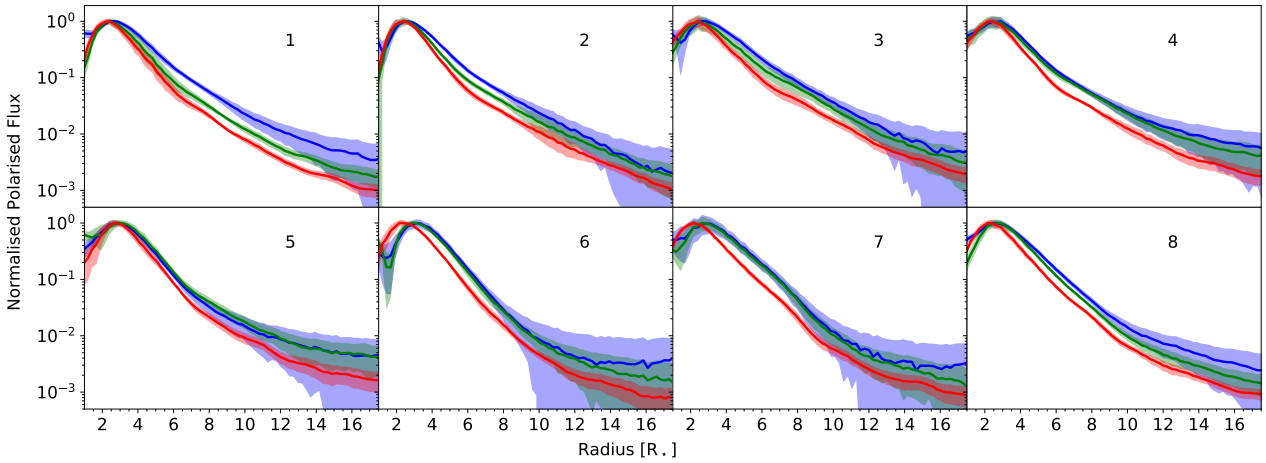

Fig. 7. Normalised radial profiles of the polarised intensity observed towards W Hya for the eight octants of the images using filters *NR* (blue), *cnt748* (green), and *cnt820* (red). The stellar radius assumed in this plot, $R_\star$, is the near-infrared stellar radius measured by Woodruff et al. (2009) of 18 mas.

absorption close to the star in filters *NR* and *cnt748*. The polarisation degree reaches peak values of 16.5, 18 and 20% in filters *NR*, *cnt748*, and *cnt820*, respectively. The three images are shown in Fig. 4

3.2.2. R Crt

The images of the polarised light around R Crt reveal a biconical outflow. This is best seen in the images of the polarisation degree shown in Fig. 5. The structure is clear in the image using filter *NR* and is still visible in those using filter *cnt748*, but not in filter *cnt820*. The polarisation degree peaks in the southern half of the biconical outflow and reaches values of 8.5% in filter *NR*, 6% in filter *cnt748*, and 4% in filter *cnt820*. We estimate the position angle of the biconical structure to be 165° ± 15° in the images in filter *NR* and 160° ± 10° in that in filter *cnt748*. These values are higher than those reported by Ishitsuka et al. (2001) for the biconical outflow traced by H_2O masers (∼150°), but given the asymmetric structure and the consequent large uncertainty in the derived position angles, the values are consistent.

3.2.3. SW Vir

As noted in Sect. 3.1.3, the PSF diffraction pattern of SW Vir strongly affects the images of the polarisation degree (Fig. 6). The PSF diffraction pattern can also be seen in the images of the polarised intensity (Fig. 3), although much less prominently. This is in principle not expected because the diffraction pattern seen in the two orthogonal polarisation directions should be the same, and should therefore be erased when the polarised intensity images are created. The explanation for the persisting diffraction pattern might reside in the fact that ZIMPOL is known to produce a small (sub-pixel) shift between the images of the two orthogonal polarisation directions (Schmid et al. 2018). This so-called beam-shift effect is well known but difficult to correct for because its strength varies between datasets, between images in the same dataset, and with telescope pointing position and rotational states of the optical components. Although the effect can be corrected for by re-aligning the images of the two polarisation components, we have not ventured into this procedure because the detailed modelling of the ZIMPOL observations of SW Vir is further complicated by the fact that the inner radius of the dust envelope is not well-resolved. Nonetheless, the observations show that the distribution of dust is not symmetric, with polarised light arising mostly from the eastern hemisphere.

3.3. Particle sizes

A general rule is that for small ($2\pi a < \lambda$, where a is the dust particle size) spherical particles, scattering is close to isotropic and the degree of polarisation is a bell-shaped curve peaking at 90° (Rayleigh scattering), while for larger particles ($2\pi a \gtrsim \lambda$) scattering becomes increasingly forward peaking and the angle-dependence of the degree of polarisation is more complex and varies strongly with particle size. Moreover, when $2\pi a \sim \lambda$ the scattering properties depend significantly on the grain models assumed. In the small-particle regime, the scattering cross section decreases with increasing wavelength.

We find that the particles that produce the polarised light around W Hya must have radii $\gtrsim$0.1 μm to reproduce the higher (or comparable) polarisation degree in the images using filter *cnt820* than in those using the other two filters. On the other hand, the higher polarisation degree in filter *NR* relative to those in the other two filters for R Crt and SW Vir favours smaller particles, with radii $\lesssim$0.1 μm. The polarisation degree towards R Crt drops by more than a factor of two between 0.65 and 0.82 μm. We note that although we make this comparison based in general considerations, the exact estimated grain sizes depend on the assumed grain model and are quite uncertain. We find that the level of polarisation degree observed towards R Crt and SW Vir is in agreement with predictions from optically thin models in visible wavelengths using the distribution of hollow spheres (DHS, Min et al. 2003) approximation with sizes <0.1 μm. We did not attempt to fit the observed spectral dependence, however. We note that the polarisation degree can differ significantly from the predictions of spheric models if scattering occurs at a small range of angles and the grains are not much smaller than the wavelength. This might be particularly important in the case of R Crt, but a better understanding of the morphology of the source is needed for more detailed model calculations.

Another interesting point is that the size of the particles around W Hya has been seen to vary with the pulsation phase of the star (Ohnaka et al. 2017). It is not clear whether a similar variation occurs for SW Vir and R Crt. We note that the light-curve amplitudes of R Crt and SW Vir are smaller and their periods are shorter than those of W Hya. This means that these stars

might present smaller variations in grain properties through their pulsation cycle. Monitoring of sources with properties similar to those of SW Vir and R Crt using ZIMPOL will help understand the mass-loss process in oxygen-rich AGB stars with low pulsation amplitudes and periods. No theoretical predictions are available for the light-phase variation of the properties of the dust particles around a star with these characteristics because wind-driving models have been calculated thus far using pulsation periods >300 days (e.g. Bladh et al. 2015; Höfner et al. 2016). Models that consider the formation of dust in outer layers of convective model stars (e.g. Höfner & Freytag 2019) will help shed light on this in the future.

4. Results and discussion

4.1. Observed morphology of the envelope of R Crt

There is a clear difference between the biconical morphology of the envelope of R Crt and the more spherical (but still asymmetrical) envelopes of W Hya and SW Vir. Because R Crt has the highest mass-loss rate of the 43 semi-regular variable AGB stars observed by Olofsson et al. (2002), the observed morphology can be an indication that either the higher mass-loss rate is produced by a peculiar process that also produces the biconical outflow, or that the inferred mass-loss rate from CO lines using a spherically symmetric model is not accurate for this source. We note that it is not clear, however, whether the biconical morphology of the circumstellar envelope close to the star also extends to larger distances where the CO lines are mainly excited. The lower mass-loss rate derived from the OH maser observations ($\sim 1 \times 10^{-7}$ $\dot{M}$ yr^{-1}, Szymczak et al. 1999) is also interesting in this context but does not help solve the problem because the derived OH shell size also depends on the assumption of a spherically symmetric and thin OH shell. The position of the SiO ring at a distance of roughly twice the near-infrared stellar radius is typical for AGB stars (e.g. Diamond et al. 1994; Cotton et al. 2004), and the observed maser spots do not trace a biconical shape. H_2O maser emission is only prominent in the south-east cone (Kim et al. 2018), which also appears brighter in polarised visible light. The unknown inclination angle precludes us from concluding whether this is caused by an asymmetry in the mass distribution between the two cones because of possible differences between forward and backward scattering. The southwest cone seems to be inclined towards the observer because H_2O maser spots are blue-shifted with respect to the velocity of R Crt.

A biconical or bipolar outflow is not common around AGB stars but is observed in a few sources, including V Hya (Sahai et al. 2003), CIT 6 (Kim et al. 2015), and WX Psc (Vinković et al. 2004). Interestingly, the mass-loss rates of these stars are all at least one order of magnitude higher than the rate derived for R Crt. The morphology is sometimes associated with the presence of a fast outflow (e.g. Sahai et al. 2003) and it is often taken as an indication of a transition into the post-AGB phase (e.g. Vinković et al. 2004). We note that there are no indications of the presence of a fast outflow in R Crt. The origin of this biconical outflow around these sources is unclear, but shaping caused by a binary companion and/or by a strong magnetic field are possible scenarios (e.g. De Marco & Izzard 2017). The current theory requires an additional source of angular momentum to explain magnetic fields in AGB stars (e.g. Nordhaus et al. 2007), which might be provided by a binary companion or even a planetary system. It is not yet clear whether the ubiquitous occurrence of magnetic fields in AGB stars can be explained solely by interactions with stellar companions (Vlemmings 2019).

Another source that shows a biconical outflow is L_2 Pup. ZIMPOL observations of this star show an edge-on disc obscuring the star in the equatorial direction but allowing visible light to escape in the polar directions. The disc might also collimate the outflow into a biconical structure (Kervella et al. 2015). The morphology of the dusty envelope of R Crt could be explained by a similar scenario to that of L_2 Pup. An obvious difference between the two sources is the expansion velocities of the outflows inferred from single-dish observations of CO lines, of 2.5 km s^{-1} for L_2 Pup and of 10 km s^{-1} for R Crt (Olofsson et al. 2002). Interestingly, observations with ALMA reveal gas expansion velocities up to ~17 km s^{-1}, which is not evident in single-dish spectra (Homan et al. 2017). Spatially resolved observations with higher sensitivity of molecular line emission towards R Crt will allow for a better comparison between these two sources.

The mass-loss rates derived based on low-excitation CO lines or dust excess may not be accurate because they are based on spherically symmetric models. If a disc that blocks stellar light, and potentially the outflow, exists in the equatorial direction around R Crt, it must be oriented nearly edge on and the biconical structure observed in scattered light must be perpendicular to it. We note, however, that no direct evidence of such a disc is seen in the ZIMPOL images we present. Moreover, Paladini et al. (2017) reported that the source has a position angle of 157° at ~10 μm, consistent with that of the biconical outflow we find. If a compact, dense disc exists around R Crt, we would have expected its signature to be seen as excess thermal dust emission in a perpendicular direction from that of the biconical outflow. ALMA observations of L_2 Pup have revealed a disc with Keplerian rotation around the star and allowed the mass of the possible planetary-mass secondary body to be constrained (Kervella et al. 2016). Equivalent observations of R Crt will help determine whether these two sources have similar morphologies of their circumstellar envelopes. Regarding the maser emission and the magnetic field orientation, a direct comparison to L_2 Pup is not possible because no spatially resolved observations of either the maser emission region or the magnetic field structure have been reported for L_2 Pup to our knowledge.

In conclusion, we are not able to determine the origin of the biconical structure seen in the circumstellar envelope of R Crt. A comparison to L_2 Pup suggests that these two sources might have a similar morphology, but no sign of a disc around R Crt is seen in either the ZIMPOL or the MIDI data. An alternative explanation, supported by the detection of a strong magnetic field in the inner part of the biconical outflow, is that magnetic fields in R Crt collimate the outflow. Further observations aimed at detecting a possible disc around R Crt and the maser morphology and magnetic field strength in L_2 Pup will help discern between these two possibilities.

4.2. Modelling of the observations of W Hya

We have calculated models to fit the observations of W Hya. The main goal was to use the polarised-intensity images to derive the radial profile of the density distribution of the grains that produce the scattered light. We did not attempt to model the polarised light observed towards R Crt and SW Vir. For R Crt, this is because of the biconical morphology of the envelope. For SW Vir, this is both because the inner radius of the envelope is not well resolved and because of the strong diffraction rings observed also in polarised light, which would complicate the modelling.

For our models of W Hya, we focused on the data obtained using filter *cnt820* because molecular and dust scattering opacities are expected to be lower in this wavelength range than in those of filters *NR* and *cnt748* (e.g. Khouri et al. 2016). Moreover, together with the images in filter *cnt748*, the images in *cnt820* show polarised light up to larger distances from the star. In Fig. 7 we show how the radial profile of the polarised intensity differs between observations using the three filters.

4.2.1. Total intensity image

We first focused on reproducing the observed size of the stellar disc of W Hya. Our model consists of a black-body, uniform-disc star and therefore does not provide a very accurate description of the observed images, which reveal significant structure (see Figs. 1 and 8). Nonetheless, the size (and shape) of the stellar disc significantly affects not only the model unpolarised-light images, but also the polarised-light and the polarisation-degree ones. Obtaining a model as accurate as possible for the stellar disc is therefore important for our analysis.

By comparing uniform-disc models with different radii to the azimuthally averaged total intensity images in the *cnt820* filter, we find that models with radii of ~3.45 au are required (see Fig. 8). This is much larger than the 1.8 au size of our reference stellar radius. This dramatic increase between infrared and visible wavelengths is caused by the thick atmosphere of molecules (and dust, as discussed below) around W Hya. As shown in the inset in Fig. 8, our model is unable to reproduce the off-centre peak of the total intensity images. This is an expected shortcoming of our model, given the simplicity of our model star.

Before comparing the models to the observations, the images were convolved with an image of a PSF-reference star. We find that the images of HD 118877 do not provide a good description of the PSF at the time of the observations of W Hya. This is most likely because of changing sky conditions between the observations of the two stars, and is evident from the different Strehl ratios obtained for the two sets of observations (see Table 2). The effect of this is clearly seen in Fig. 8 as an excess at large radii when comparing the 3.45 au model convolved with the images of HD 118877 (blue dashed line) and the observations of W Hya (solid black line). The images of p Vir (originally observed as a PSF-reference for the observations of SW Vir) were acquired at similar sky conditions to those of W Hya and therefore present a more comparable Strehl ratio. We find that using p Vir as a PSF-reference significantly improves our fits to the data at radii $\gtrsim$80 mas from the central star. Therefore, we used p Vir as the PSF-reference star in our calculations instead of HD 118877.

We find that the outflowing dust does not significantly affect the total intensity images and the derived stellar size accordingly does not depend strongly on the outflowing-dust model (especially given the simplicity of our stellar model). In this sense, there is a clear distinction in our model between dust grains residing in the high-density, gravitationally bound region (which affect the derived stellar size in the visible) and the outflowing dust. In reality, the transitions between these two regions is much more complex than our model assumes, and more detailed modelling of this transition region is necessary to better constrain the distribution of dust in this region and the effect of scattering on the stellar size in the visible.

4.2.2. Polarised intensity image

We calculated continuum radiative transfer models using the code `MCMax` (Min et al. 2009). `MCMax` treats scattering and polarisation of light using the full angle-dependent Mueller matrix and produces as output images of the Q and U parameters. We convolved these images with the image of the PSF-reference star adopted by us (p Vir) before computing the polarisation intensity and the polarisation degree images, which were then compared to the observations.

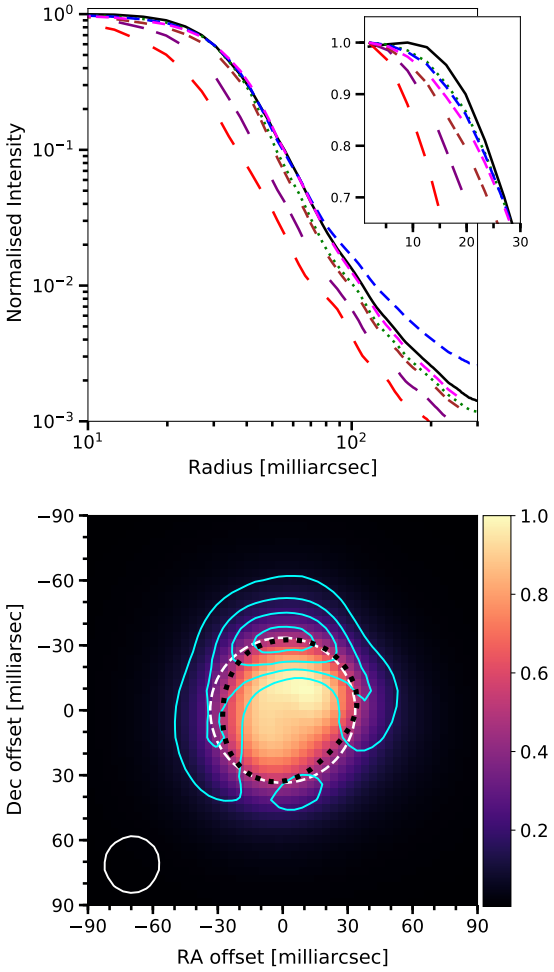

Fig. 8. Comparison between models and observations of the total intensity images in the *cnt820* filter. *Upper panel*: observed radial profile of the total intensity (full black line) compared to radial profiles derived from models convolved with the PSF-reference p Vir and considering uniform stellar discs with radii 1.86 au (long-dashed red line), 2.56 au (double-long-dashed purple line), 3.35 au (dotted green line), and 1.86 au surrounded by a dust envelope that is optically thick in the visible due to scattering extending out to 3.35 au (double-short-dashed brown line). The short-dashed blue line shows the radial profile obtained from a model with a uniform stellar disc with a radius of 3.35 au convolved with the PSF-reference HD 118877, observed following the observations of W Hya. *Lower panel*: comparison between the observed normalised total intensity (colour-scale image), the polarised intensity contours at 90, 70, 50, and 30% times the peak value (full cyan line), and the stellar disc with a radius of 3.35 au (dashed white line). The 50% levels of the images of the PSF-reference p Vir (white solid line) and of W Hya (dotted black line) are shown for reference.

We assumed a black-body star surrounded by Mg_2SiO_4 grains. We used the optical constants provided by Jäger et al. (2003) to calculate the opacities and scattering matrix based on the DHS approximation (Min et al. 2003). Our results are independent of the choice of model star because we do not fit absolute quantities, such as flux density or absolute polarised intensity, and focus only on relative quantities, such as the

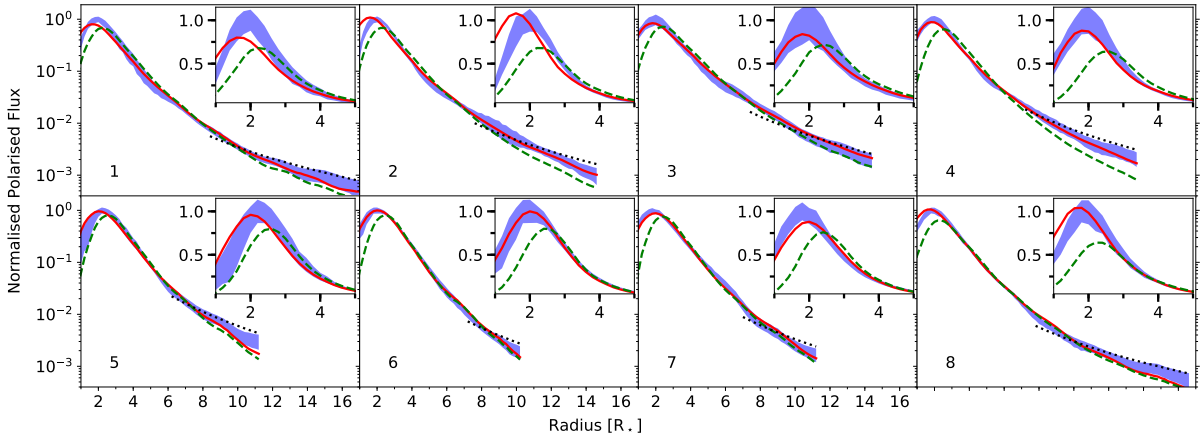

Fig. 9. Models to fit the polarised light observed towards W Hya for each of the eight octants of the image in filter *cnt820*. The observations with the 1σ error bars are shown by the shaded blue region, the full red lines show the best-fit models for each octant, the dashed green line shows the best model with a 3.45 au star, and the dotted black lines show the best-fit models with a radial power-law index $n = 2$. The stellar radius assumed in this plot, $R_\star$, is the near-infrared stellar radius measured by Woodruff et al. (2009) of 18 mas.

normalised radial profiles of the total and polarised intensities and the polarisation degree. We do not expect the choice of optical constants to significantly affect the results because the other reasonable choices of dust species ($MgSiO_3$ and Al_2O_3) have scattering properties that are similar to those of Mg_2SiO_4. We chose the DHS grain model (with an irregularity parameter $f_{max} = 0.8$) because it has been shown to produce a good fit to the scattering properties of real particles measured in the laboratory (Min et al. 2005). The model dust envelopes we calculated are spherically symmetric and irradiated by a central star.

4.2.3. Radial profile of the dust density

Our modelling approach is similar to that employed by Khouri et al. (2016) for modelling ZIMPOL observations of R Dor. We divided the observed images into octants and fit the azimuthal average of the observed radial profiles of the polarised light for each octant. We numbered the octants from one to eight starting with the octant delimited by the north and north-west direction and proceeding clockwise. The uncertainties in the observed radial profiles are given by the combination of the uncertainty on the polarised intensity per pixel (given by the ESO pipeline) and of the standard deviation of the polarised intensity between pixels at a same given radial distance. We ranked the models based on the χ^2 of the fits to the data. The uncertainties on the derived parameter values were calculated by considering all models that produce χ^2 values that are lower than $\chi^2_{best} + \sqrt{2\nu}$, where χ^2_{best} is the lowest χ^2 value obtained and ν is the number of degrees of freedom in the χ^2 calculation.

We find that the choice of grain size (within the range we explored, 0.1 to 0.5 μm) and the grain composition (Mg_2SiO_4, $MgSiO_3$, or Al_2O_3) has a much weaker effect than the dust density profile on the radial profile of the polarised intensity. For simplicity, we therefore modelled the radial profiles using only Mg_2SiO_4 grains with sizes of 0.1 μm, as determined by Ohnaka et al. (2017).

The radial dust-density profile of the outflow in our models is described by the power law $\rho(r) = \rho_\circ\,(R_\circ/r)^{-n}$, where $\rho_\circ$ is the dust density at the inner radius of the dust outflow $R_\circ$. We are unable to reproduce the observed peak of the radial profile of the polarised intensity with a model with a radius of 3.45 au, which is required to fit the total intensity images. This is because the minimum possible value of $R_\circ$ (3.45 au) is too high. The only way we could improve the fit to the observations in the context of our model was to substitute the central source by a smaller star surrounded by an optically thick scattering dust shell with an outer radius of 3.45 au. Such a shell produces sufficient polarised light to shift the peak of the polarised intensity to smaller radii, providing a much better fit to the observations (see Fig. 9). For all the octants, the models with a star surrounded by an optically thick shell provide χ^2 values lower by more than a factor of two than the models with a 3.45 au star and no optically thick dust shell. By comparing the brightness distributions of the polarised and unpolarised intensity (as shown in Fig. 8), it is evident that indeed the polarised flux peaks very close to or even within the photosphere at 0.82 μm.

The large size of the central source implies that $R_\circ$ is effectively a fixed parameter in our fitting procedure because it is always set to 3.45 au. Therefore, the only free parameters are the exponent n, the normalisation of the radial profile of the polarised intensity, and the ratio between the dust density immediately inside and outside the optically thick dust shell. Our models are insensitive to the inner radius and dust density in the optically thick inner shell, provided that the shell is optically thick. Considering 0.1 μm grains, our models require dust densities in the optically thick dust shell of $\gtrsim 2 \times 10^{-16}$g cm^3 and a dust density decrease by a factor between 30 and 100 at the outer edge of the optically thick shell. To place better constraints on the dust distribution in this region, a model that includes the contribution of absorption and scattering by molecules is necessary.

The resulting best-fitting models are shown in Fig. 9, and the interpolated best-fitting values for the parameters and the uncertainties are given in Table 3. Our fitting results suggest that n varies significantly between the different octants, $3.0 \lessapprox n \lessapprox 4.8$. The asymmetry of the dust envelope can be inferred directly from Fig. 4 by noting that the polarisation degree drops below 2% at shorter distances to the east than to the west, even if the polarisation degree close to the star is higher to the east than to the west. To reproduce the observed polarisation degree, the outwards radial optical depths required by our models outside of the optically thick shell vary between ~0.5 and ~1 for the octants that display minimum and maximum polarised light.

The derived steepness of the dust density profile depends not only on the acceleration profile of the outflow, but also on the contrast between the amount of grains in the high-gas-density extended atmosphere (which is gravitationally bound)

Table 3. Radial distances of the regions compared to the models for each octant in the cnt820 images.

Oct	r [mas]	RPI	n	$\chi^2_{\rm min}$	ν	$R^{\rm exp2.0}_{\rm min}$ [mas]
1	280	1.7	3.40 ± 0.3	37.3	70	137
2	250	1.0	3.35 ± 0.2	63.7	58	122
3	230	0.7	3.00 ± 0.4	10.9	57	119
4	230	0.6	3.00 ± 0.3	22.0	53	115
5	180	0.6	4.00 ± 0.4	26.5	44	97
6	180	0.9	4.80 ± 0.3	17.6	36	115
7	180	1.0	4.10 ± 0.2	30.0	41	112
8	280	1.7	3.85 ± 0.2	55.7	68	130

Notes. We also present the relative peak intensity at each octant (RPI) relatively to the peak intensity of the azimuthal average of the entire image. $R^{\rm exp2.0}_{\rm min}$ is the radius up to which the radial dust density profile is inconsistent with a non-accelerating steady-state wind.

and the number of grains in the accelerating wind (where radiation pressure has overcome gravity). Determining the density and velocity distribution of the gas in these inner regions at the time of ZIMPOL observations will allow for a much more complete picture of the acceleration region of the given AGB outflow. The dynamical timescale for the dust grains at these distances is about a few years (assuming $\upsilon_{\rm dust} = 15$ km s^{-1}) and the timescale for variation of the dust distribution in the innermost regions seems to be about a month. Therefore, observations of the time variability of the dust density distribution around W Hya over a few months are expected to provide important additional constraints.

Our results also imply that dust might form already inside the visible photosphere at radii <1.9 $R_\star$. This would not be at odds with theoretical models (e.g. Höfner et al. 2016), but implies that inner radii of scattering dust envelopes derived from this type of observations should be viewed as upper limits. The high values of the dust density required by our models of the optically thick dust shell suggest that at least part of the opacity is due to molecular absorption or scattering. Whether the observed scattered light can be partially explained by scattering of light by molecules in the high-gas-density regions close to the W Hya (~10^{11} mol cm^{-3}, Vlemmings et al. 2017) needs to be investigated in future studies.

We also considered the possibility that the peak of the polarised intensity is shifted to smaller radii because of instrumental effects that produce spurious polarised light. One known effect that can significantly affect the polarised signal close to the star in ZIMPOL observations is the beam shift (Schmid et al. 2018). We find no evidence for significant beam-shift effect in the observations of W Hya, therefore we consider this an unlikely cause for the shift in polarised-intensity peak to smaller radii in the cnt820 images.

Multi-wavelength imaging or interferometry observations provide crucial information for the interpretation of our results. For instance, Ireland et al. (2004) observed W Hya at a pulsation phase 0.44 with the Masked Aperture-Plane Interference Telescope in the Anglo-Australian Telescope to determine the size of the stellar disc of W Hya at wavelengths between 680 and 930 nm. The authors found that the stellar size increased smoothly towards the blue, instead of abruptly within molecular bands, and suggested that the observed photosphere of W Hya at visible wavelengths must be significantly affected by dust scattering. We note that our model with an optically thick dust shell is unable to reproduce the increase in stellar size between 0.82 and 0.75 μm. However, obtaining a fit with our spherically symmetric model to the images using the *cnt748* filter is difficult because of the higher contrast between the brightness at the centre of the stellar disc and the off-centre emission peak. Moreover, the importance of dust grains for the total opacity and for determining the size of the stellar photosphere is expected to be relatively larger in a spectral region without strong molecular features, such as the region covered by the *cnt820* filter employed by us. Molecules are expected to have a stronger effect on the appearance of the photosphere at 0.65 and 0.75 μm.

Ohnaka et al. (2017) also modelled ZIMPOL observations of W Hya similar to those presented by us and were able to reproduce the position of the peak of the polarised intensity. However, the authors did not reproduce the size of the stellar disc and considered a star with a radius of ~1.8 au, which our results show might lead to inconsistencies. The inner radius of the dust envelope derived by them (2.3 au) is smaller than the size of the stellar photosphere at 0.82 μm determined by us.

4.2.4. Extent of the acceleration region around W Hya

Independently of the best power-law fit, we also investigated the minimum radius from which a $\rho(r) \propto r^{-2}$ density law is consistent with the data, $R^{\rm exp2.0}_{\rm min}$. This was done by calculating the cumulative χ^2 starting from the outer edge of each octant and proceeding inwards in radius for a model with $n = 2$. The outer edge was defined as the radius at which the polarisation degree dropped below 2% (see Table 3), while $R^{\rm exp2.0}_{\rm min}$ was defined as the radius at which the χ^2 value deviated more than 3σ from the expected value given the number of points considered and the associated errors. The motivation for this calculation is that the dust density radial profile of a steady-state outflow should transition from the steep profile observed close to the star ($n > 2$) to a profile with $n = 2$ when the wind reaches terminal velocity. In this way, $R^{\rm exp2.0}_{\rm min}$ is a lower limit to the outer radius of the dust-acceleration region.

Our results show that the $\rho(r) \propto r^{-2}$ density law expected for an outflow expanding at constant velocity is not consistent with the observations for $r \lesssim 100$ mas. Therefore the acceleration of the wind is expected to happen at least up to a radius of ~100 mas, which is expected. These are lower limits for the radius from which the dust particles are no longer accelerated. For the direction in which polarised light is seen up to larger distances, we find that density law with $n = 2$ is not consistent with the observations up to $r \approx 137$ mas. When we consider the stellar radius in the infrared of 18 mas (Woodruff et al. 2009), this distance corresponds to $r \approx 7.5\ R_\star$. These lower limits are still consistent with theoretical predictions for the wind-acceleration region (e.g. Höfner 2008), which predict an acceleration region extending to ~12 $R_\star$. This shows that high-angular-resolution observations of polarised light are very close to directly testing model predictions for the wind acceleration in AGB stars.

5. Summary and conclusions

We presented ZIMPOL observations of W Hya, R Crt, and SW Vir, which show mass-loss rates between 10^{-7} and 10^{-6} $M_\odot$ yr^{-1} and relatively small visual light amplitudes (between 1.4 and 2.8 mag). The images in polarised light show very different morphologies of the inner dust envelopes. Particularly, R Crt shows a biconical circumstellar envelope which had been previously seen in observations of maser emission. The

cause for this peculiar morphology is not clear, but we speculate that it might be caused by interactions with a binary companion and/or strong magnetic fields. This object might provide important insight into how the shaping of biconical outflows takes place.

The polarisation degree observed toward R Crt decreases sharply between 0.65 and 0.82 μm, while for SW Vir and W Hya the observed values are more similar. In the case of W Hya, the polarisation degree is maximum at 0.82 μm. Ohnaka et al. (2017) modelled observations towards W Hya at a similar phase and derived grains sizes of 0.1 μm. The observations we report suggest that the grains around SW Vir are $\lesssim$0.1 μm and those around R Crt are smaller <0.1 μm than those around W Hya. This indication must be confirmed using radiative transfer modelling. It is not clear whether this reflects a fundamental difference because the size of the grains around W Hya has been seen to vary from ~0.1 to ~0.5 μm from minimum to maximum light phase (Ohnaka et al. 2017). The more regular and larger amplitude pulsations of W Hya in comparison to R Crt and SW Vir might cause the properties of the dust grains to vary more strongly. Monitoring observations of low-amplitude pulsators will help shed light on this issue.

The stronger polarised signal is detected towards W Hya, and we are able to see scattered light out to ~17 infrared stellar radii. Our observations show that a significant amount of polarised light is produced within the visible photosphere. We are able to reproduce this by considering models with an inner dust shell that is optically thick to scattering. This suggests that inner radii derived from this type of observations should only be regarded as upper limits. Moreover, we find that the density of dust grains drops steeply outside the photosphere, most likely tracing the transition between extended atmosphere and accelerating outflow. We are able to determine lower limits to the extent of the acceleration region and find that acceleration occurs until at least 7 infrared stellar radii. This is consistent with predictions from theoretical models, which find that outflows accelerate up to ~12 stellar radii. Our findings highlight the power of ZIMPOL in imaging dust in the crucial dust-formation and wind-acceleration region around AGB stars.

Acknowledgements. We thank the anonymous referee whose careful reading of the manuscript and thoughtful suggestions significantly contributed to improve the quality of the paper. This work was supported by ERC consolidator grant 614264. E.D.B. acknowledges financial support from the Swedish National Space Agency. Based on observations collected at the European Southern Observatory under ESO programme 096.D-0930.

References

Adam, C., & Ohnaka, K. 2019, A&A, 628, A132
Bladh, S., & Höfner, S. 2012, A&A, 546, A76
Bladh, S., Höfner, S., Aringer, B., & Eriksson, K. 2015, A&A, 575, A105
Bladh, S., Paladini, C., Höfner, S., & Aringer, B. 2017, A&A, 607, A27
Bowers, P. F., & Johnston, K. J. 1994, ApJS, 92, 189
Cotton, W. D., Mennesson, B., Diamond, P. J., et al. 2004, A&A, 414, 275
Cox, N. L. J., Kerschbaum, F., van Marle, A.-J., et al. 2012, A&A, 537, A35
Danilovich, T., Lombaert, R., Decin, L., et al. 2017, A&A, 602, A14
Decin, L., Richards, A. M. S., Waters, L. B. F. M., et al. 2017, A&A, 608, A55
De Marco, O., & Izzard, R. G. 2017, PASA, 34, e001
Diamond, P. J., Kemball, A. J., Junor, W., et al. 1994, ApJ, 430, L61
Gail, H.-P., Scholz, M., & Pucci, A. 2016, A&A, 591, A17
Gobrecht, D., Cherchneff, I., Sarangi, A., Plane, J. M. C., & Bromley, S. T. 2016, A&A, 585, A6
Habing, H. J., & Olofsson, H. 2003, Asymptotic Giant Branch Stars (Berlin: Springer)
Herpin, F., Baudry, A., Thum, C., Morris, D., & Wiesemeyer, H. 2006, A&A, 450, 667
Höfner, S. 2008, A&A, 491, L1
Höfner, S., & Freytag, B. 2019, A&A, 623, A158
Höfner, S., & Olofsson, H. 2018, A&ARv, 26, 1
Höfner, S., Bladh, S., Aringer, B., & Ahuja, R. 2016, A&A, 594, A108
Homan, W., Richards, A., Decin, L., et al. 2017, A&A, 601, A5
Ireland, M. J., Tuthill, P. G., Bedding, T. R., Robertson, J. G., & Jacob, A. P. 2004, MNRAS, 350, 365
Ishitsuka, J. K., Imai, H., Omodaka, T., et al. 2001, PASJ, 53, 1231
Jäger, C., Dorschner, J., Mutschke, H., Posch, T., & Henning, T. 2003, A&A, 408, 193
Jura, M., & Kleinmann, S. G. 1992, ApJS, 83, 329
Kamiński, T., Wong, K. T., Schmidt, M. R., et al. 2016, A&A, 592, A42
Kamiński, T., Müller, H. S. P., Schmidt, M. R., et al. 2017, A&A, 599, A59
Karovicova, I., Wittkowski, M., Ohnaka, K., et al. 2013, A&A, 560, A75
Kervella, P., Montargès, M., Lagadec, E., et al. 2015, A&A, 578, A77
Kervella, P., Homan, W., Richards, A. M. S., et al. 2016, A&A, 596, A92
Khouri, T., de Koter, A., Decin, L., et al. 2014a, A&A, 561, A5
Khouri, T., de Koter, A., Decin, L., et al. 2014b, A&A, 570, A67
Khouri, T., Waters, L. B. F. M., de Koter, A., et al. 2015, A&A, 577, A114
Khouri, T., Maercker, M., Waters, L. B. F. M., et al. 2016, A&A, 591, A70
Khouri, T., Vlemmings, W. H. T., Olofsson, H., et al. 2018, A&A, 620, A75
Kim, H., Liu, S.-Y., Hirano, N., et al. 2015, ApJ, 814, 61
Kim, D.-J., Cho, S.-H., Yun, Y., et al. 2018, ApJ, 866, L19
Kiss, L. L., Szatmáry, K., Cadmus, Jr. R. R., & Mattei, J. A. 1999, A&A, 346, 542
Kozasa, T., & Sogawa, H. 1997, Ap&SS, 251, 165
Lawson, P. R. 2000, Principles of Long Baseline Stellar Interferometry (Pasadena, CA: JPL Publication)
Lebzelter, T., & Hron, J. 2003, A&A, 411, 533
Maercker, M., Schöier, F. L., Olofsson, H., Bergman, P., & Ramstedt, S. 2008, A&A, 479, 779
McMullin, J. P., Waters, B., Schiebel, D., Young, W., & Golap, K. 2007, ASP Conf. Ser., 376, 127
Min, M., Hovenier, J. W., & de Koter, A. 2003, A&A, 404, 35
Min, M., Hovenier, J. W., & de Koter, A. 2005, A&A, 432, 909
Min, M., Dullemond, C. P., Dominik, C., de Koter, A., & Hovenier, J. W. 2009, A&A, 497, 155
Mondal, S., & Chandrasekhar, T. 2005, AJ, 130, 842
Nordhaus, J., Blackman, E. G., & Frank, A. 2007, MNRAS, 376, 599
Norris, B. R. M., Tuthill, P. G., Ireland, M. J., et al. 2012, Nature, 484, 220
Ohnaka, K., Weigelt, G., & Hofmann, K.-H. 2016, A&A, 589, A91
Ohnaka, K., Weigelt, G., & Hofmann, K.-H. 2017, A&A, 597, A20
Olofsson, H., González Delgado, D., Kerschbaum, F., & Schöier, F. L. 2002, A&A, 391, 1053
Paladini, C., Klotz, D., Sacuto, S., et al. 2017, A&A, 600, A136
Percy, J. R., Wilson, J. B., & Henry, G. W. 2001, PASP, 113, 983
Plane, J. M. C. 2013, Phil. Trans. R. Soc. A, 371, 20120335
Ridgway, S. T., Jacoby, G. H., Joyce, R. R., Siegel, M. J., & Wells, D. C. 1982, AJ, 87, 808
Sahai, R., Morris, M., Knapp, G. R., Young, K., & Barnbaum, C. 2003, Nature, 426, 261
Schmid, H. M., Bazzon, A., Milli, J., et al. 2017, A&A, 602, A53
Schmid, H. M., Bazzon, A., Roelfsema, R., et al. 2018, A&A, 619, A9
Schmidtke, P. C., Africano, J. L., Jacoby, G. H., Joyce, R. R., & Ridgway, S. T. 1986, AJ, 91, 961
Szymczak, M., Cohen, R. J., & Richards, A. M. S. 1999, MNRAS, 304, 877
Takigawa, A., Kamizuka, T., Tachibana, S., & Yamamura, I. 2017, Sci. Adv., 3, eaao2149
van Belle, G. T., Lane, B. F., Thompson, R. R., et al. 1999, AJ, 117, 521
van Leeuwen, F. 2007, A&A, 474, 653
Vinković, D., Blöcker, T., Hofmann, K.-H., Elitzur, M., & Weigelt, G. 2004, MNRAS, 352, 852
Vlemmings, W. H. T. 2019, Proc. IAU Symp. 343
Vlemmings, W. H. T., van Langevelde, H. J., Diamond, P. J., Habing, H. J., & Schilizzi, R. T. 2003, A&A, 407, 213
Vlemmings, W., Khouri, T., O'Gorman, E., et al. 2017, Nat. Astron., 1, 848
White, N. M., & Feierman, B. H. 1987, AJ, 94, 751
Wing, R. F. 1971, PASP, 83, 301
Woitke, P. 2006, A&A, 460, L9
Woodruff, H. C., Ireland, M. J., Tuthill, P. G., et al. 2009, ApJ, 691, 1328
Young, K., Phillips, T. G., & Knapp, G. R. 1993, ApJ, 409, 725
Zhao-Geisler, R., Quirrenbach, A., Köhler, R., Lopez, B., & Leinert, C. 2011, A&A, 530, A120
Zhao-Geisler, R., Quirrenbach, A., Köhler, R., & Lopez, B. 2012, A&A, 545, A56